

Stratospheric balloon observations of infrasound waves from the January 15 2022 Hunga eruption, Tonga

Aurélien Podglajen¹, Alexis Le Pichon², Raphaël F. Garcia³, Solène Gérier³,
Christophe Millet², Kristopher Bedka⁴, Konstantin Khlopenkov⁵, Sergey
Khaykin⁶, Albert Hertzog⁷

¹Laboratoire de Météorologie Dynamique (LMD/IPSL), École polytechnique, Institut polytechnique de
Paris, Sorbonne Université, École normale supérieure, PSL Research University, CNRS, Paris, France

²CEA, DAM, DIF, 91297 Arpajon, France

³Institut Supérieur de l'Aéronautique et de l'Espace (ISAE-SUPAERO), Université de Toulouse, 10 Ave
E. Belin 31400 Toulouse, France

⁴NASA Langley Research Center, Hampton, Virginia, USA

⁵Science Systems and Applications, Inc., Hampton, Virginia, USA

⁶Laboratoire Atmosphères, Observations Spatiales (LATMOS), UVSQ, Sorbonne Université, CNRS,
IPSL, Guyancourt, France

⁷Laboratoire de Météorologie Dynamique (LMD/IPSL), Sorbonne Université, École polytechnique, Institut
polytechnique de Paris, École normale supérieure, PSL Research University, CNRS, Paris, France

Key Points:

- Comparison between balloon-borne and ground-based observations of infrasound waves triggered by the January 2022 Hunga eruption
- Eruption sequence from infrasound in broad agreement with plume top height evolution
- Benchmark for long-range monitoring of infrasound from large explosive sources using stratospheric balloon observations

Abstract

The 15 January 2022 eruption of the Hunga volcano (Tonga) generated a rich spectrum of waves, some of which achieved global propagation. Among numerous platforms monitoring the event, two stratospheric balloons flying over the tropical Pacific provided unique observations of infrasonic wave arrivals, detecting five complete revolutions. Combined with ground measurements from the infrasound network of the International Monitoring System, balloon-borne observations may provide additional constraint on the scenario of the eruption, as suggested by the correlation between bursts of acoustic wave emission and peaks of maximum volcanic plume top height. Balloon records also highlight previously unobserved long-range propagation of infrasound modes and their dispersion patterns. A comparison between ground- and balloon-based measurements emphasizes superior signal-to-noise ratios onboard the balloons and further demonstrates their potential for infrasound studies.

Plain Language Summary

The eruption of the Hunga volcano on January 15 2022 was one of the most powerful blasts of the last century. This fast and strong perturbation of the atmosphere triggered atmospheric waves which were followed around the world multiple times. Here, we use records of sound waves emitted by the eruption from two balloons flying at about 20 km altitude over the Pacific combined with ground stations around the volcano to help characterize the event and its scenario. Due to weak relative wind and turbulence, the sounds on the balloon are generally clearer than on the ground, demonstrating the potential of high-altitude measurements for extreme events.

1 Introduction

While the 2021-2022 eruptive phase of Hunga volcano (Tonga) started in mid-December 2021, the paroxysmal explosion occurred on January 15th 2022 around 04:16 UTC (Poli & Shapiro, 2022). Over the next hour, the volcanic plume penetrated deep into the atmosphere, reaching the stratopause and beyond (up to 58 km), whereas the umbrella cloud spread at approximately 35 km to form a 600 km diameter disk (Carr et al., 2022; Proud et al., 2022). The altitude of volcanic overshoots, the height and extent of the umbrella cloud set a new record for volcanic eruptions over the satellite era, overtaking Mount Pinatubo and its maximum reported plume height of 40 km (Holasek et al., 1996). The plume generated a large perturbation of the stratospheric aerosol layer and stratospheric composition (Millán et al., 2022), with likely substantial radiative impacts (Sellitto et al., 2022).

Besides triggering globally detected surface seismic waves (Poli & Shapiro, 2022) and tsunamis in several oceanic basins (Yuen et al., 2022; Matoza et al., 2022), the Hunga eruption also excited a wide spectrum of atmospheric waves, which were observed radiating away from the volcano (Matoza et al., 2022). These include the edge Lamb wave (Matoza et al., 2022; Wright et al., 2022), internal gravity waves (Wright et al., 2022; Ern et al., 2022) and infrasound (Matoza et al., 2022; Vergoz et al., 2022). The Lamb wave amplitude (> 11 hPa peak-to-peak near Hunga) and propagation pattern are in particular reminiscent of the wave trains observed following the historical 1883 Krakatoa eruption (Matoza et al., 2022).

Most observations of Hunga waves were obtained by remote-sensing instruments or surface (micro)barometers, whereas the plume extended above stratospheric altitudes. In this paper, we present unique measurements of infrasound wave trains recorded in the stratosphere onboard two long-duration balloons flying over the Pacific. While balloon-borne instruments also detected acoustic signals corresponding to the early eruptive sequence of Hunga, including the January 13 explosion, the present study focuses on analyzing the waves triggered by the main eruption on January 15. We describe the first

and multiple-revolution wave arrivals in balloon data and compare them to ground-based observations. Then, we discuss how infrasound may provide additional information on the eruption chronology and the value of balloon-borne measurements for this and similar events.

2 Data and Methods

2.1 Strateole-2 balloon data

In the frame of the Strateole-2 project (Haase et al., 2018), 17 superpressure balloons (SPBs) were launched from Seychelles by the French space agency (CNES) in October-December 2021. Strateole-2 SPBs are constant-volume balloons designed to fly several months at a chosen density level in the tropical upper troposphere-lower stratosphere (between 18.5 and 21 km). On January 15 2022, two SPBs (STR1 and TTL4) remained over the tropical Pacific at about 19 km above sea level. Their altitudes and approximate locations are given in Table 1 and displayed in Fig. 1 a); both balloons drifted horizontally following the wind, which for infrasound implies negligible Doppler shift but changes the distance to source with time.

Among various instruments, all Strateole-2 payloads notably include the TSEN temperature and pressure sensors (Hertzog et al., 2007) and a GPS. Position is measured every 30 s with 1 m vertical resolution. The pressure sensor (Paroscientific-6000-15A) samples at 1 Hz with 100 mPa resolution. It has a flat frequency response over the range of interest (up to 0.25 Hz).

SPBs undergo vertical oscillations forced by atmospheric motions and modulated by the balloon's response (Massman, 1978; Vincent & Hertzog, 2014). Due to the background vertical pressure gradient, such vertical motions induce additional apparent pressure fluctuations compared to measurements obtained at constant altitude. To correct for this effect, we remove the component of pressure fluctuations due to the hydrostatic pressure gradient to derive the Eulerian (constant-altitude) pressure perturbation p :

$$p = p_l \exp\left(\frac{g}{R_d T} \zeta'\right) - \bar{p} \quad (1)$$

where p_l and T are the raw (balloon-following) pressure and temperature, \bar{p}_l the time-averaged pressure, ζ' geopotential height anomalies, $g = 9.81 \text{ m s}^{-2}$ and $R_d = 287 \text{ J/K/kg}$. GPS position is interpolated at 1 s to compute ζ' and p . The effect of correction 1, described in Supplement S1, is significant at frequencies around that of the balloon oscillations ($\sim 4.5 \text{ mHz}$) or lower, but for infrasound frequencies above $\sim 0.02 \text{ Hz}$, p closely follows p_l . The precision of the pressure data is sufficient to detect the energy peak of the oceanic microbarom around 0.2 Hz (Bowman & Lees, 2018).

2.2 IMS microbarometer data

Infrasound stations from the International Monitoring System (IMS) of the Comprehensive Nuclear-Test-Ban Treaty Organization are arrays of microbarometers sensitive to acoustic pressure variations between 0.02 and 4 Hz with a flat frequency response (e.g., Hupe et al., 2022). We use data from 5 stations listed in Table 1 and located either in the vicinity of the balloons or at distances of 1,800-4,000 km from Hunga (Fig. 1 a). A thorough investigation of Hunga infrasound waves in IMS data is presented in Vergoz et al. (2022).

2.3 Ancillary dataset: geostationary satellite data

We also employ stereoscopic 10-minute-resolution cloud top height retrievals to infer the chronology of the eruption. These data are derived at NASA Langley using the

Table 1. Receiver coordinates and infrasound properties in ground-based and balloon-based records.

receiver	distance (km)	Latitude °N	Longitude °E	altitude (km)	c_g (m/s)	Observed T_L (30-40 mHz) with respect to IS22 (dB)		
						WP1	WP2	WP3
IS07	5227	-19.93	134.33	ground	297.00	-15.66	-14.04	-37.19
IS22	1849	-22.18	166.85	ground	297.00	0.00	0.00	0.00
IS24	2755	-17.75	-149.30	ground	261.00	-28.27	ND	ND
IS36	2699	-43.92	176.48	ground	300.00	-15.82	-16.02	-28.11
IS40	3957	-4.10	152.10	ground	301.00	-22.72	-15.89	-28.67
IS57	8645	33.61	-116.45	ground	292.00	-35.72	-23.67	-33.18
STR1	2238	-0.80	-171.64	20.5	279.00	-14.89	-12.68	-24.75
TTL4	7640	15.70	-116.02	18.5	276.00	-26.41	-22.75	-36.62

ND: Wavepacket not discernible at receiver.

117 parallax between almost-synchronized 10.3 μm -band brightness temperature images ob-
 118 tained from different viewing angles by the geostationary satellites GOES-17 (Eastern
 119 Pacific sector) and Himawari-8 (Western Pacific sector). For the Hunga plume, the spa-
 120 tial resolution of the product is about 6 km and its vertical accuracy typically lies be-
 121 tween 0.2-0.4 km. Further description of the retrieval method is provided in Supplement S2.

122 2.4 Numerical simulations of infrasound attenuation

123 In a horizontally isotropic medium, the modulus $|P|$ (ducted) wave pressure am-
 124 plitude varies along propagation path due to geometric spreading, following (e.g., Pierce
 125 & Posey, 1971):

$$|P|(d, z) = \sqrt{\frac{\rho \sin(d_r/a)}{\rho_r \sin(d/a)}} |\tilde{P}|(z) \quad (2)$$

126 where a is the Earth radius, d the horizontal distance (range) from Hunga (d_r an arbi-
 127 trary reference distance), ρ the density, ρ_r a reference density ($\rho_r = 1.2 \text{ kg/m}^3$ except
 128 if stated otherwise) and the density- and range-scaled pressure amplitude $|\tilde{P}|$ a priori
 129 depends only on altitude z . Note that this vertical scaling only retains the density fac-
 130 tor in sonic impedance $I = \rho c$, since variations of the sound speed factor c are over-
 131 shadowed by the vertical structure of the mode for long-range horizontal propagation.
 132 Equation 2 also neglects leakage and absorption. Most importantly, the assumed isotropic
 133 propagation breaks for infrasound waves which are sensitive to the stratospheric wind
 134 fields (Matoza et al., 2022; Vergoz et al., 2022).

135 To apprehend expected infrasound amplitude evolution for different azimuths, we
 136 compute (linear) attenuation at a given frequency using the range-dependent parabolic
 137 equation (PE) solver NCPA-ePape(Waxler et al., 2021). The model assumes planar prop-
 138 agation along the orthodromes and the influence of wind is encapsulated into an effec-
 139 tive sound celerity c_{eff} . c_{eff} sections along each great-circle path are defined by:

$$c_{\text{eff}}(d, z) = \sqrt{\gamma R_d T(d, z)} + \mathbf{u}_h(d, z) \cdot \mathbf{e}_x(d, z), \quad (3)$$

140 with γ the capacity ratio, T the temperature, \mathbf{u}_h the horizontal wind vector and \mathbf{e}_x the
 141 range-dependent unit vector pointing from the source towards the receiver. c_{eff} profiles,
 142 calculated from the European Center for Medium-range Weather Forecast (ECMWF)
 143 ERA5 reanalysis (Hersbach et al., 2020), are shown in Fig. 1 b). Above 60 km and up
 144 to 140 km, ECMWF profiles are merged with temperature and wind climatologies (MSISE00
 145 and HWM14, Picone et al., 2002; Drob et al., 2015) perturbed by a range-dependent

146 realization of a gravity-wave field prescribed following Gardner et al. (1993). For the lower
 147 boundary condition, we assume a rigid ground (infinite impedance). T_L transmission losses
 148 (T_L) between Hunga and the sensors are quantified in dB, i.e.:

$$T_L(d, z) = 20 \log_{10} \left(\frac{|P|(d, z)}{|P|(d = d_r, z = z_r)} \right) \quad (4)$$

149 where z and z_r are the receiver and reference altitude. Figure 1 c), d), e) presents sec-
 150 tions of scaled transmission loss \tilde{T}_L (calculated using Eq. 4 and scaled pressure $|\tilde{P}|$) and
 151 curves of regular T_L from NCPA-ePape. Results highlight expected anisotropic propa-
 152 gation. In the spirit of comparing signal-to-noise ratios (SNR) onboard balloons and on
 153 the ground, keeping the $\rho^{-\frac{1}{2}}$ factor has its merits, since possible sources of dynamical
 154 noise at high altitude (i.e., balloon or gondola wake encounters) scale with density and
 155 dominate over altitude-independent electronic noise (Krishnamoorthy et al., 2020a).

156 Note that, as stressed by Matoza et al. (2022), directly interpreting Hunga infra-
 157 sound attenuation quantitatively using PE is difficult due to various uncertainties aris-
 158 ing in this peculiar case, including a complex source, possible invalidity of the underly-
 159 ing approximations discussed in Waxler and Assink (2019) and biases in wind field from
 160 climatology, gravity-wave perturbation or even reanalysis (e.g. Podglajen et al., 2014).
 161 Hence, PE simulations are only used here as a pedagogical tool to contextualize differ-
 162 ences between receivers.

163 3 Results

164 3.1 First infrasound arrivals

165 Pressure spectrograms during the first overpass of the waves (Fig. 2) show arriv-
 166 ing first the low-frequency Lamb wave pulse (Matoza et al., 2022; Vergoz et al., 2022;
 167 Wright et al., 2022) extending up to ~ 3 mHz. Above ~ 10 mHz, instead of a single dom-
 168 inant pulse several receivers (e.g., IS22, STR1, Fig. 2) recorded a complex infrasound ar-
 169 rival sequence within which one may identify at least three distinct initial wavepackets
 170 (WPs) peaking around 20-30 mHz. WPs onsets, separated by periods of reduced acous-
 171 tic power, are highlighted in Fig 2. The delay between WP1&3 is without ambiguity be-
 172 yond the spread in arrival times which can be expected for acoustic wave generated by
 173 a unique trigger. As for WP1&2, the roughly constant time separation observed among
 174 receivers at different short-range distances and azimuths from Hunga (IS22, STR1), to-
 175 gether with the absence of similar duplication of WP3, rules out differential propaga-
 176 tion. Overall, this suggests that the WPs originate from successive source-level events.
 177 Dispersion, however, manifests itself at larger distances, creating longer, duplicated wavepack-
 178 ets at TTL4 (in particular WP3).

179 Taking advantage of the reproducible and highly structured arrival sequence, we
 180 deduced approximate average travel speed c_g for the different sensors, as explained in
 181 Supplement S2. c_g values (Table 1) vary consistently with prevailing stratospheric wind
 182 conditions (weakest to the East of the volcano, strongest to the West). Back-propagating
 183 WPs to the source suggests pulses of emission around 04:15, 04:53 and 08:27 (± 5 min-
 184 utes). This chronology will be further discussed in Sect. 4.1.

185 10-minute-averaged spectra at the arrival of WP1 (Fig. 2 a, b) show a significant
 186 enhancement over the whole acoustic range compared to the period immediately prior
 187 to it, with a peak around 20-30 mHz, especially striking for balloon sensors. WP2 has
 188 somewhat higher frequency, peaking around 30-40 mHz in balloon records.

189 Besides distinct WPs, balloon observations exhibit a lasting tail of enhanced acous-
 190 tic variability above 0.01 Hz with a return to pre-eruption levels after about a day. This
 191 feature is akin to the Coda observed in seismic waves (e.g. Aki, 1997) and likely results

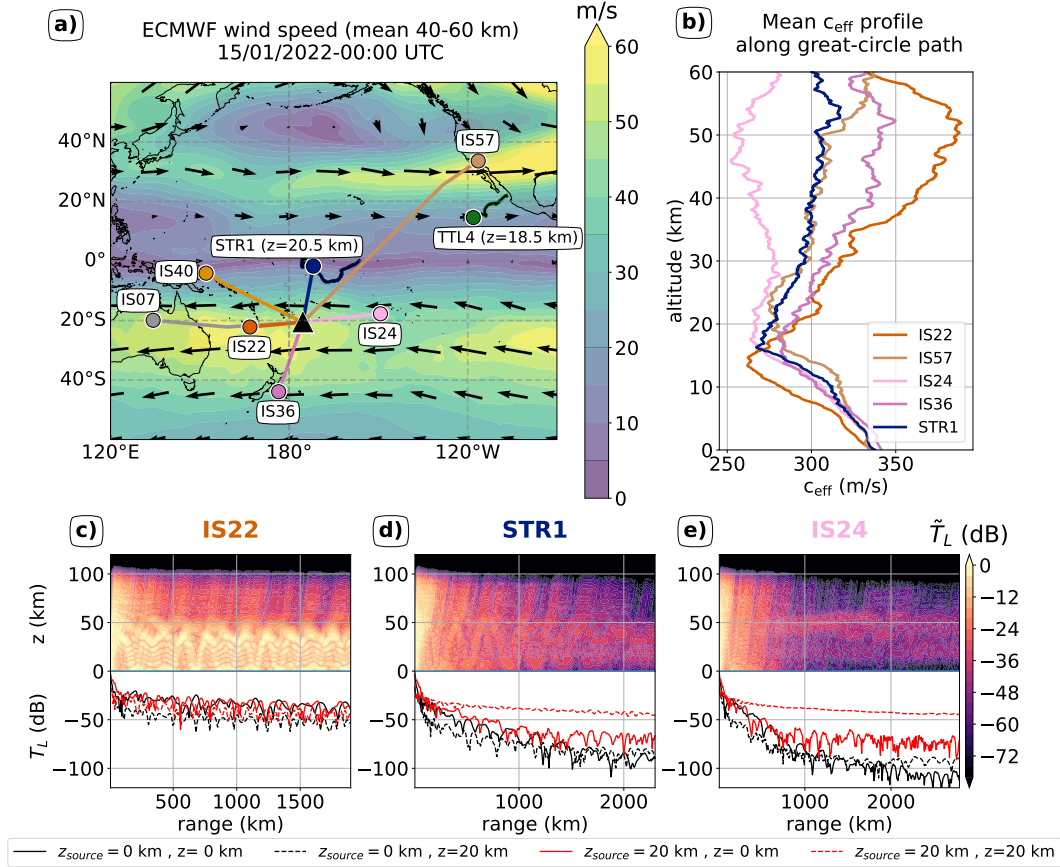


Figure 1. (a) Upper-stratospheric (40-60 km average) horizontal wind direction (vectors) and speed (contours) on January 15 2022 from ECMWF. Colored dots represent the location of the ground stations and balloons at the time of the main blast, with (colored lines) Hunga-to-receiver orthodromes. Balloon trajectories from the eruption until the termination of the flights are shown in black. (b) Average effective sound speed profile along selected orthodromes in (a). Panels (c), (d), (e) (top) Along-path sections of scaled transmission loss \tilde{T}_L with respect to $d_r = 17.5$ km, $z_r = z_{source}$ in the directions of IS22, STR1 and IS21 computed for a ground source of frequency 0.05 Hz. (Bottom) Transmission loss profiles T_L at the ground (solid lines) and 20 km a.s.l. (dashed lines) for a point source at the ground (black) and 20 km (red).

192 from multipathing and wave scattering by small-scale inhomogeneities, e.g. pre-existing
193 gravity waves (Chunchuzov et al., 2011).

194 3.2 Anisotropy of infrasound propagation

195 A large spread in infrasound-signal amplitude is found among receivers, as sum-
196 marized in Table 1, which reports observed transmission losses with respect to IS22 for
197 the 3 WPs. This results from the variability of along-path stratospheric winds near Hunga
198 (Fig. 1 (a)), which imply large variations in the associated c_{eff} profiles (Fig. 1 (b)) and
199 infrasound ducting efficiency.

200 To illustrate this, selected T_L sections, estimated with ePape for a ground source
201 of frequency 0.05 Hz, are displayed in Fig. 1. Towards IS22, strong tailwinds support a
202 stratospheric duct from ~ 50 km down to the ground (Fig 1 c), explaining low atten-
203 uations for receivers West of the volcano (IS07, IS36, IS40). In other directions (STR1,
204 IS24), head- and crosswinds hamper propagation at the surface. Nevertheless, a shal-
205 lower duct exists, tied to the temperature minimum around the tropopause and confined
206 to the upper troposphere-lower stratosphere (UTLS). We will refer to it as the UTLS
207 duct. This duct generates larger scaled amplitudes $|\tilde{P}|$ at stratospheric balloon flight al-
208 titude (Fig 1 d, e).

209 Despite the qualitative agreement with Table 1 for each WP taken separately, this
210 reasoning does not explain the observed increase in IS22-relative attenuations from WP1
211 to WP3. As reported by Matoza et al. (2022), the scatter in T_L is also smaller than in
212 PE simulations forced at ground level. Besides dispersion, model biases and violated as-
213 sumptions (e.g., linearity), these discrepancies likely partly arise due to the complexity
214 of the time-varying source (Matoza et al., 2022). While a detailed assessment is beyond
215 the scope of our study, we note that a possible (but not sole) contributing factor may
216 be the event-dependent vertical distribution of the forcing. Indeed, Figure 1 suggests that
217 significant generation at upper levels (here 20 km) tends to reduce anisotropy compared
218 to lower-level sources.

219 3.3 Multiple revolutions of acoustic waves

220 Longer recordings over the days following the eruption reveal successive revolutions
221 of infrasound waves (Vergoz et al., 2022), as shown for the balloons and nearby stations
222 IS22 and IS57 in Fig. 3. In the following, we adopt the convention for multiple passages
223 of Matoza et al. (2022); Vergoz et al. (2022): A1 for the direct (short-orthodrome) ar-
224 rival, A2 for the first antipodal arrival, A3 for A1 + one revolution etc. Ground mea-
225 surements are polluted by sporadic bursts of noise related to atmospheric turbulences,
226 which prevent detections under high surface-wind conditions beyond A1 (Vergoz et al.,
227 2022). A clearer picture emerges from balloon observations (Fig. 3 (b), (d)), which al-
228 most exclusively exhibit geophysical signals above 30 mHz, and record clear arrivals up
229 to A10 at STR1.

230 Figure 3 e-n highlights distinct acoustic dispersion patterns in Fig. a-d, which are
231 described in the following. Although dispersion mixes A2 and A3 at STR1 (Fig. 3 e),
232 one can clearly distinguish an A2 wavetrain with virtually no dispersion ("compact mode")
233 retaining the imprint of the source (i.e., distinct WP1 and WP2) over several revolutions.
234 This mode has typical round-the-world-transit speed of 288 m/s (± 1 m/s). It is visible
235 only at STR1, at least for passages A2 and A4 (Fig. 3 f). On Fig. 3 e), second wavetrain
236 ("dispersive modes") follows. It is typically slower (~ 275 m/s), mixes with A3, and fea-
237 tures two dispersion lines around 20 mHz and 70 mHz. A double dispersion line was also
238 observed for A1 in Kenya ($d = 15,750$ km) (Vergoz et al., 2022). The 70 mHz disper-
239 sive mode is also evident in passages A2 and A4 at TTL4 (Fig. 3 g and i) but absent at
240 IS57 (Fig. 3 l and n). The lower dispersion curve is longer-lived and appears at least at

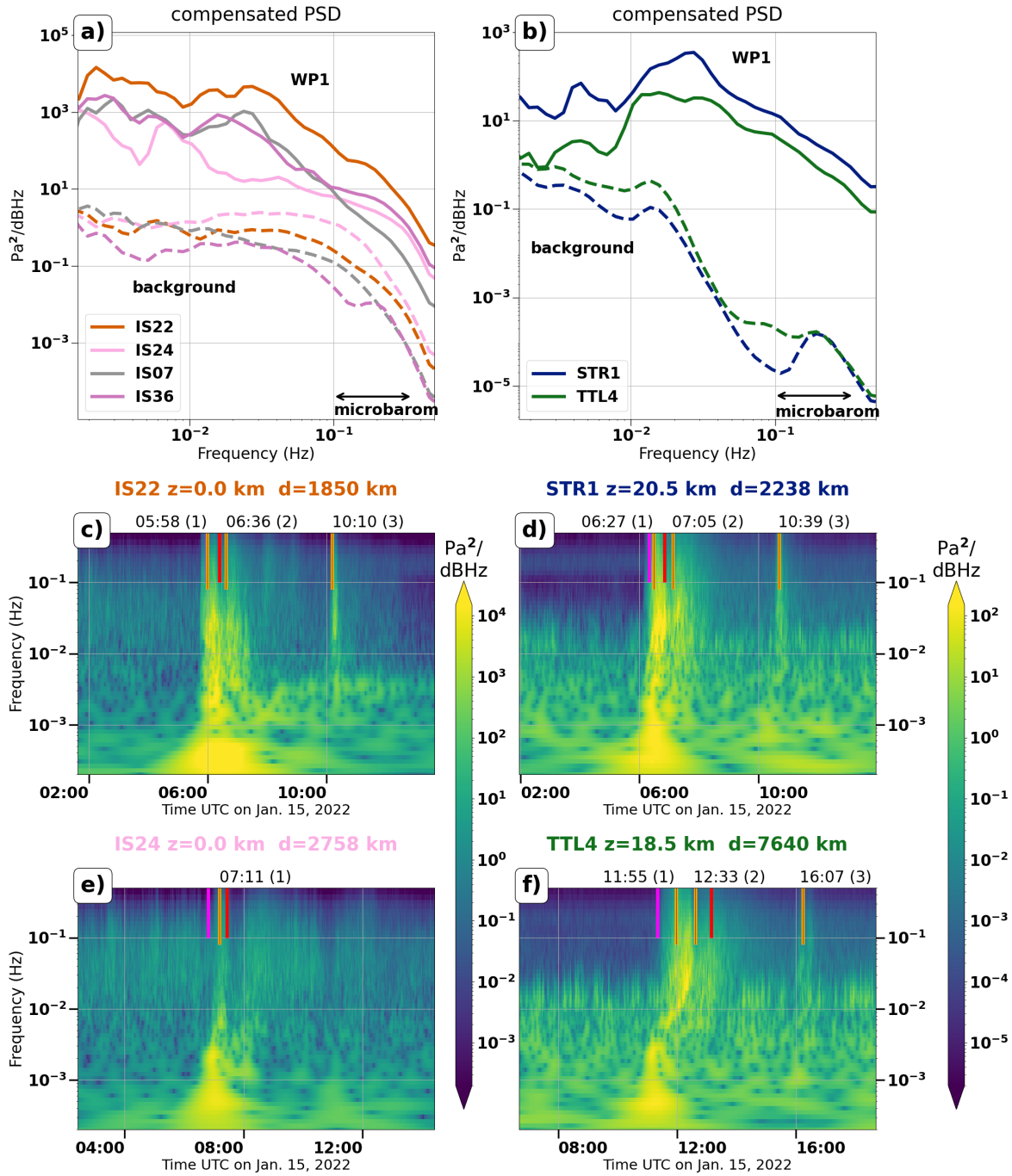


Figure 2. Compensated power spectral density (PSD multiplied by frequency) during the overpass of WP1 (solid line) and background of the 3 hours before the eruption (dashed line) for (a) the ground stations and (b) the balloons. c), d), e), f) Selected spectrograms of the pressure signals corresponding to the first wave arrivals. The orange vertical lines indicate arrival times of WPs (timings reported above). Purple and red lines correspond to expected arrival times for the first event (see text) assuming travel speeds $c_g = 300\text{m/s}$ and $c_g = 240\text{m/s}$, respectively.

241 A2-4 at TTL4 and A2-10 at STR1, as well as at IS22 and IS57. From the spectrograms
 242 (Fig. 3 a)), we estimate $\frac{\partial c_g}{\partial \omega} \simeq -500\text{-}600$ m for this mode, for which the decrease in
 243 travel speed with frequency results in a flattening of the wave trains in frequency-time
 244 space over successive circumnavigations (Fig. 3 a-d)). Finally, for completeness, a non-
 245 dispersive 30-mHz wavepacket was recorded for A3 at TTL4, although not at IS57 (Fig. 3
 246 h-m).

247 The nature of this family of modes remains unclear. Their typical celerity resem-
 248 bles stratosphere-ducted infrasound with wind bringing substantial contribution in one
 249 or the other direction. Contrasted efficiency of wind ducting in different propagation di-
 250 rections likely plays a role in the favored "antipodal" propagation of the dispersive modes
 251 found at TTL4. It is noteworthy that, whereas ground stations IS22 measures larger am-
 252 plitudes for A1, the situation reverses for later overpasses. For instance, the signal am-
 253 plitude near the lower dispersion curve for passages A2 and A4 seems systematically larger
 254 at balloon altitude. Some arrivals clearly detected in the balloon signals are not discernible
 255 in ground recordings (e.g., at TTL4, the upper dispersion line for A2 and A4 or the A3
 256 arrival). Altogether, this suggests that long-lived modes are ducted at upper levels, al-
 257 though their vertical structure and the role of wind in supporting them warrants further
 258 investigations.

259 4 Discussion

260 4.1 Infrasound emission and chronology of the eruption

261 In Sect. 3.1, we argued that STR1 and IS22 captured the same infrasound emis-
 262 sion sequence. The inferred scenario is substantiated in Fig. 4, which depicts shifted time
 263 series of 3-minute 30-40 mHz-filtered (a) signal variance (proportional to acoustic power)
 264 and (b) scaled amplitude for selected receivers. High correlations with IS22 are seen for
 265 other shorter-range sensors at various distances West of Hunga (IS07, IS40, IS36). They
 266 benefit from limited dispersion effects, likely thanks to the source proximity and over-
 267 all similar (and favorable) propagation conditions (Vergoz et al., 2022). In contrast, sig-
 268 nals are less distinct East of Hunga (IS24). Interestingly, balloon STR1 exhibits the high-
 269 est correlation with IS22 around WP1&2 and has similar scaled amplitude $|\tilde{P}|$.

270 Distinct WPs likely mirror different phases of acoustic-wave emission at the source.
 271 Vergoz et al. (2022) found that infrasound and seismic wave activity coincide for the early
 272 part of the eruption but decouple at later stages (i.e., WP 3). In very different eruptive
 273 contexts, previous studies (e.g., Fee et al., 2010) have found a correlation between ra-
 274 diated acoustic power and plume height. To explore this link with volcanic aerial activ-
 275 ity, Figure 4 a) presents the evolution of maximum plume altitude from stereoscopic cloud
 276 top height (CTH) retrievals during the eruption. Notwithstanding a ~ 20 -minute delay
 277 between the onsets of infrasound WPs and observations of plumes reaching their ceil-
 278 ing, a rough match may be found between (i) WP1 and the first plume reaching the meso-
 279 sphere (04:37), and (ii) WP3 and a later plume observed reaching 38 km at 08:47. The
 280 higher initial plume also seems associated with larger infrasound power (Fig. 4) and smaller
 281 anisotropy (Sect. 3.2) than the lower-height 08:47 injection. Contrary to WP1 and 3, ten-
 282 tative attribution of WP2 is not obvious. The second extended mesospheric intrusion
 283 occurs slightly West of Hunga and closely follows the first in time. CTH data also in-
 284 dicate a 48-km overshoot at Hunga's location at 05:17 which may better correspond. Event
 285 identification is challenging and not always meaningful given the complexity of the plume
 286 evolution and sources at play. Nevertheless, the general comparison tends to suggest a
 287 significant role of processes related to plume dynamics (Woulff & McGetchin, 1976; Ma-
 288 toza et al., 2009; Fee & Matoza, 2013; Watson et al., 2022) in Hunga infrasound gener-
 289 ation. It highlights the value of STR1's records which, gathered inside a waveguide, ap-
 290 pear well-placed for source characterization.

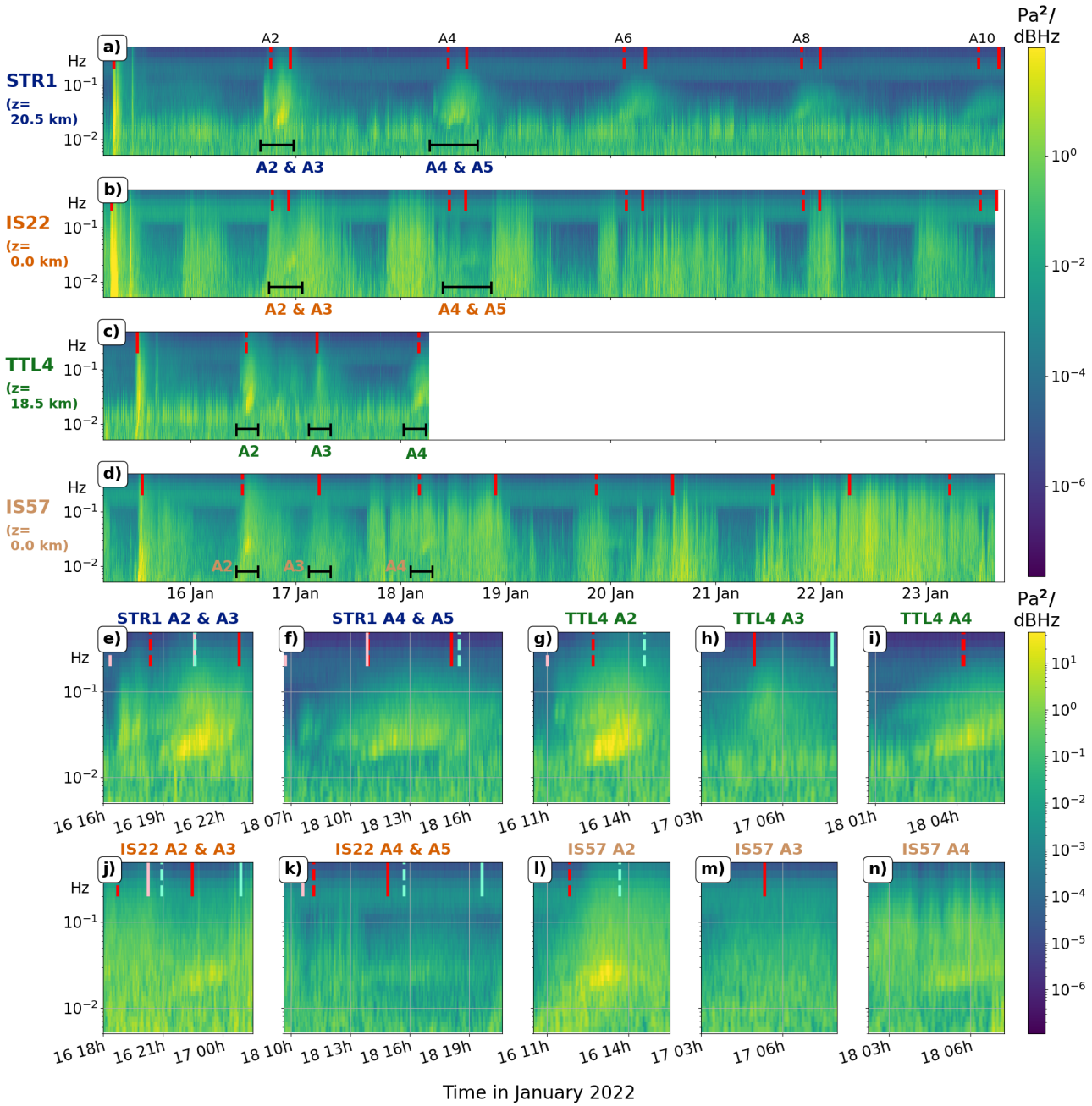


Figure 3. Spectrograms of the pressure signals at balloons a) STR1 and c) TTL4 and ground stations b) IS22 and d) IS57. Expected arrival times are shown for the 275 (red) m/s travel speed (solid lines for "direct", dashed for antipodal). TTL4 time series stop on January 18 due to its burst. e) to n) Zoom on the (e, g, j, l) first antipodal arrival and (e, h, m) second direct and (f, i) antipodal arrivals at (e to i) the balloons and (j to n) ground stations. Direct and antipodal arrivals superpose partly at STR1 and IS22. Further expected arrival times for 290 (pink) and 260 (light green) m/s are displayed.

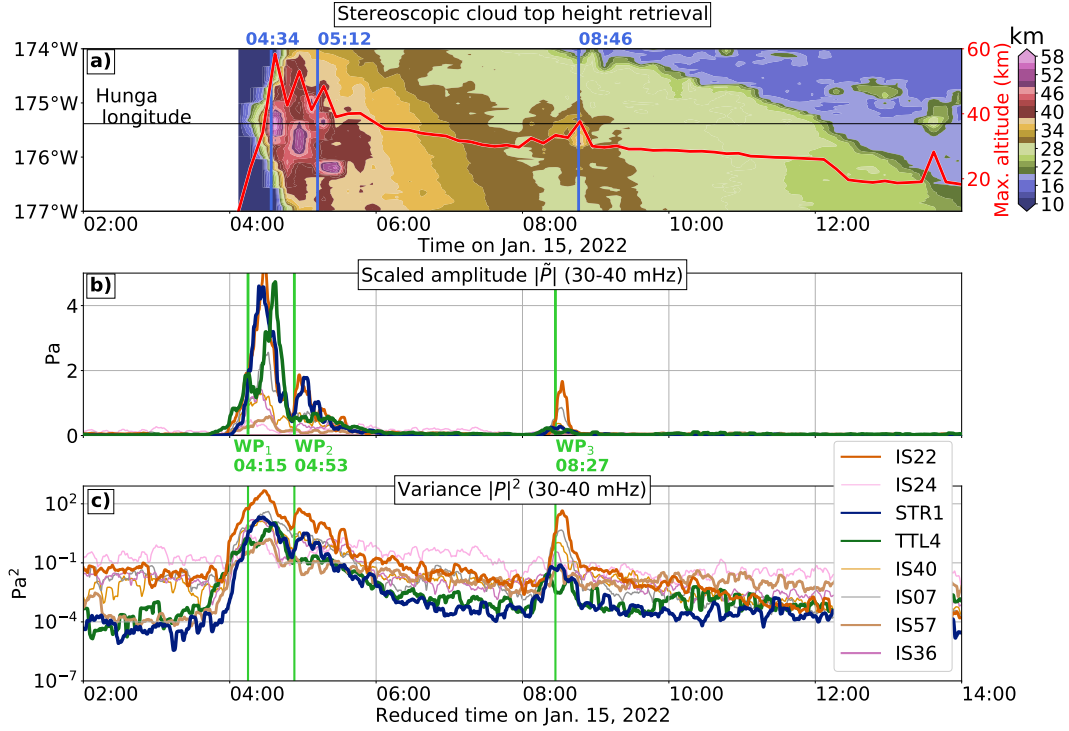


Figure 4. (a) Hovmöller diagram of plume top altitude and (red line) time series of maximum plume height in the area (20.75°S-20.35°S, 175.7°W-175.3°W). (b) 3-minute scaled pressure amplitude $|\tilde{P}|$ time series (30-40 mHz filtered) for selected receivers. The reference in Eq. 2 is here chosen at STR1 ($\rho_r = 0.08 \text{ kg/m}^3$, $d_r = 2,210 \text{ km}$). (c) 3-minute $|P|$ variance (30-40 mHz). Green vertical lines are time onsets of WPs, and blue ones are the same shifted by 19 minutes. The time axis represents range-corrected reduced time $t_r = t - \frac{d}{c_g}$, c_g from Table 1.

291 The presented scenario of intermittent aerial activity is generally consistent with
 292 other atmospheric records of the event (e.g., Astafyeva et al., 2022; Vergoz et al., 2022;
 293 Wright et al., 2022). For example, ground pressure measurements at Nukua’lofa (Tonga,
 294 $d = 64$ km) show 4 major pressure minima (Wright et al., 2022), 3 of which closely match
 295 our WPs (04:36, 05:10 and 08:46). However, no enhanced infrasound corresponds to the
 296 third minimum ($\sim 05:51$).

297 4.2 Advantages and potential limitations of balloon measurements

298 Our study evidences an infrasound signal-to-noise ratio (SNR) improved by a fac-
 299 tor of at least 10 at lower stratospheric altitudes compared to the ground (Fig. 2 a, b
 300 and 4). Reasons include (1) the location of the receiver inside the UTLS waveguide and
 301 (2) reduced noise in the absence of wind relative to the sensor (Bowman & Lees, 2015;
 302 Bowman & Krishnamoorthy, 2021; Krishnamoorthy et al., 2020b).

303 For a ground source, infrasound signals are larger at the surface in conditions sup-
 304 porting deep propagation (West of Hunga). However, upper-air reception appears favored
 305 in otherwise unfavorable propagation conditions (IS21, Fig. 1 (e)). In general, the strong
 306 anisotropy observed for ground receivers is mitigated at UTLS levels, an advantage re-
 307 inforced for sources around the UTLS duct (Fig. 1 (e)). It is exacerbated in the case of
 308 Hunga for long-range paths from multiple circumnavigations, for which larger signals are
 309 encountered in the stratosphere.

310 Ground-level winds exceeding a few m/s (Vergoz et al., 2022) typically result in
 311 a background noise level ($|P|^2$) about 3 orders of magnitude larger at IMS stations than
 312 recorded onboard the balloons, as shown in Fig. 4). Turbulence-induced noise is a well-
 313 known challenge of ground-based infrasound monitoring (e.g., Marty, 2019). Under low
 314 surface winds, reduced noise at the ground may be associated with better SNR there,
 315 as detailed in Supplement S4.

316 Despite its assets, the balloon platform might suffer from specific biases. One is re-
 317 lated to the balloons oscillations (Massman, 1978), which are only partially corrected by
 318 the current implementation of Eq. 1 (see Supplement S1 for further discussion). Oth-
 319 ers may be unanticipated. For instance, Garcia et al. (2022) recently identified a mis-
 320 match between balloon observations and pressure fluctuations expected from large-incidence
 321 infrasound generated by seismic waves. Those authors ruled out resonant excitation of
 322 pendulum oscillations and proposed that the observed discrepancies are induced by move-
 323 ments of the balloon/gondola system. For Hunga infrasound, we argue that the repeated
 324 recordings of continuous dispersion curves in the infrasound range between 10 and 100
 325 mHz (Fig. 3) advocate against large artifacts related to resonance at specific frequen-
 326 cies, demonstrating that pressure measurements onboard balloons are quantitatively re-
 327 liable for shallow-incident-angle infrasound waves.

328 5 Conclusions

329 The cataclysmic January 15 2022 eruption of the Hunga volcano triggered a wide
 330 spectrum of atmospheric waves unprecedented in modern observational records. Located
 331 2,200 and 7,800 km away from the volcano, two long-duration stratospheric balloons mea-
 332 sured a clear signature of the surface-guided Lamb wave and of infrasound waves. Sup-
 333 ported by plume top height data, the first arrival of infrasound wave packets at frequen-
 334 cies between 0.02 and 0.05 Hz indicate several bursts of acoustic wave emission highlight-
 335 ing a complex eruption scenario. Later infrasound arrivals associated with multiple rev-
 336 olutions (up to A10) could be detected until the end of the flights, 9 days after the erup-
 337 tion, corresponding to wavepackets circumnavigating the globe 5 times.

338 Together with balloon-borne infrasound earthquake (Brissaud et al., 2021; Garcia
 339 et al., 2022), surface (Bowman & Albert, 2018; Young et al., 2018) and underground (Bowman
 340 & Krishnamoorthy, 2021) explosion detections, this exceptionally long-range detection
 341 of acoustic waves from the Hunga eruption demonstrates the potential of long-duration
 342 stratospheric balloons for the monitoring of natural and anthropogenic hazards. Short-
 343 comings of the 2021 Strateole-2 infrasound payload are (1) the limited time resolution
 344 of pressure measurements (1 Hz) and (2) the lack of azimuth and incidence angle mea-
 345 surements. The former will be improved in future campaigns by increasing the sampling
 346 rate of pressure measurements. For the latter, different teams recently tried to cover the
 347 gap with IMUs (Garcia et al., 2020; Bowman et al., 2022) or antennas of pressure sen-
 348 sors (Krishnamoorthy et al., 2019; Garcia et al., 2020). We recommend including such
 349 dedicated instrumentation in the future to provide additional constraint on wave prop-
 350 erties. Finally, the response of SPBs to high-frequency atmospheric excitations is prone
 351 to significant uncertainties (Podglajen et al., 2016; Garcia et al., 2022). Further theo-
 352 retical investigations are warranted to improve inferences on atmospheric wave proper-
 353 ties from this invaluable platform (Bowman et al., 2022).

354 6 Open Research

355 Strateole-2 data is available at [https://data.ipsl.fr/catalog/strateole2/eng/
 356 catalog.search#/search?from=1&to=30](https://data.ipsl.fr/catalog/strateole2/eng/catalog.search#/search?from=1&to=30). IMS data is available upon request at [https://
 357 www.ctbto.org/specials/vdec](https://www.ctbto.org/specials/vdec) (last accessed on 2022-05-11). ECMWF data can be
 358 found at [https://cds.climate.copernicus.eu/cdsapp#!/dataset/reanalysis-era5-
 359 -pressure-levels?tab=form](https://cds.climate.copernicus.eu/cdsapp#!/dataset/reanalysis-era5-pressure-levels?tab=form) (last accessed on 2022-05-11). GOES-17 and Himawari-
 360 8 datasets are publicly accessible through Amazon Web Services (AWS). AWS Open Data
 361 description pages: <https://registry.opendata.aws/noaa-goes/> and [https://registry
 362 .opendata.aws/noaa-himawari/](https://registry.opendata.aws/noaa-himawari/).

363 Acknowledgments

364 The authors thank Daniel Bowman, David Fee and Alex Iezzi for insightful reviews, and
 365 Alain Hauchecorne and François Lott for discussions. The sponsorship of CNES, CNRS-
 366 INSU and NSF to Strateole-2 balloon activities is gratefully acknowledged.

367 References

- 368 Aki, K. (1997). Seismic Coda Waves: A Stochastic Process in Earth’s Lithosphere.
 369 In S. A. Molchanov & W. A. Woyczynski (Eds.), *Stochastic Models in Geosys-
 370 tems* (pp. 1–24). New York, NY: Springer. doi: 10.1007/978-1-4613-8500-4_1
- 371 Astafyeva, E., Maletckii, B., Mikesell, T. D., Munaibari, E., Ravanelli, M., Coisson,
 372 P., . . . Rolland, L. (2022). The 15 January 2022 Hunga Tonga Eruption His-
 373 tory as Inferred From Ionospheric Observations. *Geophysical Research Letters*,
 374 *49*(10), e2022GL098827. doi: 10.1029/2022GL098827
- 375 Bowman, D. C., & Albert, S. A. (2018, June). Acoustic event location and back-
 376 ground noise characterization on a free flying infrasound sensor network in
 377 the stratosphere. *Geophysical Journal International*, *213*(3), 1524–1535. doi:
 378 10.1093/gji/ggy069
- 379 Bowman, D. C., & Krishnamoorthy, S. (2021). Infrasound From a Buried Chemical
 380 Explosion Recorded on a Balloon in the Lower Stratosphere. *Geophysical Re-
 381 search Letters*, *48*(21), e2021GL094861. doi: 10.1029/2021GL094861
- 382 Bowman, D. C., & Lees, J. M. (2015). Infrasound in the middle stratosphere mea-
 383 sured with a free-flying acoustic array. *Geophysical Research Letters*, *42*(22),
 384 10,010–10,017. doi: 10.1002/2015GL066570
- 385 Bowman, D. C., & Lees, J. M. (2018). Upper Atmosphere Heating From Ocean-
 386 Generated Acoustic Wave Energy. *Geophysical Research Letters*, *45*(10), 5144–

- 387 5150. doi: 10.1029/2018GL077737
- 388 Bowman, D. C., Rouse, J. W., Krishnamoorthy, S., & Silber, E. A. (2022, May).
 389 Infrasound direction of arrival determination using a balloon-borne aeroseis-
 390 mometer. *JASA Express Letters*, 2(5), 054001. doi: 10.1121/10.0010378
- 391 Brissaud, Q., Krishnamoorthy, S., Jackson, J. M., Bowman, D. C., Komjathy, A.,
 392 Cutts, J. A., ... Walsh, G. J. (2021). The First Detection of an Earthquake
 393 From a Balloon Using Its Acoustic Signature. *Geophysical Research Letters*,
 394 48(12), e2021GL093013. doi: 10.1029/2021GL093013
- 395 Carr, J. L., Horváth, Á., Wu, D. L., & Friberg, M. D. (2022). Stereo Plume
 396 Height and Motion Retrievals for the Record-Setting Hunga Tonga-Hunga
 397 Ha'apai Eruption of 15 January 2022. *Geophysical Research Letters*, 49(9),
 398 e2022GL098131. doi: 10.1029/2022GL098131
- 399 Chunchuzov, I. P., Kulichkov, S. N., Popov, O. E., Waxler, R., & Assink, J. (2011,
 400 October). Infrasound scattering from atmospheric anisotropic inhomoge-
 401 neities. *Izvestiya, Atmospheric and Oceanic Physics*, 47(5), 540–557. doi:
 402 10.1134/S0001433811050045
- 403 Drob, D. P., Emmert, J. T., Meriwether, J. W., Makela, J. J., Doornbos, E., Conde,
 404 M., ... Klenzing, J. H. (2015). An update to the Horizontal Wind Model
 405 (HWM): The quiet time thermosphere. *Earth and Space Science*, 2(7), 301–
 406 319. doi: 10.1002/2014EA000089
- 407 Ern, M., Hoffmann, L., Rhode, S., & Preusse, P. (2022). The mesoscale gravity
 408 wave response to the 2022 tonga volcanic eruption: Airs and mls satellite
 409 observations and source backtracing. *Geophysical Research Letters*, 49(10),
 410 e2022GL098626. Retrieved from [https://agupubs.onlinelibrary.wiley](https://agupubs.onlinelibrary.wiley.com/doi/abs/10.1029/2022GL098626)
 411 [.com/doi/abs/10.1029/2022GL098626](https://doi.org/10.1029/2022GL098626) (e2022GL098626 2022GL098626) doi:
 412 <https://doi.org/10.1029/2022GL098626>
- 413 Fee, D., Garces, M., & Steffke, A. (2010, June). Infrasound from Tungurahua Vol-
 414 cano 2006–2008: Strombolian to Plinian eruptive activity. *Journal of Volcanol-
 415 ogy and Geothermal Research*, 193(1), 67–81. doi: 10.1016/j.jvolgeores.2010.03
 416 .006
- 417 Fee, D., & Matoza, R. S. (2013, January). An overview of volcano infrasound: From
 418 hawaiian to plinian, local to global. *Journal of Volcanology and Geothermal
 419 Research*, 249, 123–139. doi: 10.1016/j.jvolgeores.2012.09.002
- 420 Garcia, R. F., Klotz, A., Hertzog, A., Martin, R., Grier, S., Kassarian, E., ... Mi-
 421 moun, D. (2022). Infrasound from large earthquakes recorded on a network
 422 of balloons in the stratosphere. *Geophysical Research Letters*, n/a(n/a),
 423 e2022GL098844. Retrieved from [https://agupubs.onlinelibrary.wiley](https://agupubs.onlinelibrary.wiley.com/doi/abs/10.1029/2022GL098844)
 424 [.com/doi/abs/10.1029/2022GL098844](https://doi.org/10.1029/2022GL098844) (e2022GL098844 2022GL098844) doi:
 425 <https://doi.org/10.1029/2022GL098844>
- 426 Garcia, R. F., Martire, L., Chaigneau, Y., Cadu, A., Mimoun, D., Portus, M. B.,
 427 ... Martin, R. (2020, December). An active source seismo-acoustic experi-
 428 ment using tethered balloons to validate instrument concepts and modelling
 429 tools for atmospheric seismology. *Geophysical Journal International*, 225(1),
 430 186–199. Retrieved from <https://doi.org/10.1093/gji/ggaa589> doi:
 431 10.1093/gji/ggaa589
- 432 Gardner, C. S., Hostetler, C. A., & Franke, S. J. (1993). Gravity wave models for
 433 the horizontal wave number spectra of atmospheric velocity and density fluc-
 434 tuations. *Journal of Geophysical Research: Atmospheres*, 98(D1), 1035–1049.
 435 doi: 10.1029/92JD02051
- 436 Haase, J., Alexander, M. J., Hertzog, A., Kalnajs, L., Deshler, T., Davis, S., ...
 437 Venel, S. (2018). Around the World in 84 Days. *EOS*. doi: 10.1029/
 438 2018eo091907
- 439 Hersbach, H., Bell, B., Berrisford, P., Hirahara, S., Horányi, A., Muñoz-Sabater, J.,
 440 ... Thépaut, J.-N. (2020). The ERA5 global reanalysis. *Quarterly Journal of
 441 the Royal Meteorological Society*, 146(730), 1999–2049. doi: 10.1002/qj.3803

- 442 Hertzog, A., Cocquerez, P., Guilbon, R., Valdivia, J.-N., Venel, S., Basdevant, C.,
 443 ... Schmitt, É. (2007, December). Stratéole/Vorcore—Long-duration, Super-
 444 pressure Balloons to Study the Antarctic Lower Stratosphere during the 2005
 445 Winter. *Journal of Atmospheric and Oceanic Technology*, *24*(12), 2048–2061.
 446 doi: 10.1175/2007JTECHA948.1
- 447 Holasek, R. E., Self, S., & Woods, A. W. (1996). Satellite observations and inter-
 448 pretation of the 1991 mount pinatubo eruption plumes. *Journal of Geo-
 449 physical Research: Solid Earth*, *101*(B12), 27635–27655. Retrieved from
 450 <https://agupubs.onlinelibrary.wiley.com/doi/abs/10.1029/96JB01179>
 451 doi: <https://doi.org/10.1029/96JB01179>
- 452 Hupe, P., Ceranna, L., Le Pichon, A., Matoza, R. S., & Mialle, P. (2022). Inter-
 453 national monitoring system infrasound data products for atmospheric studies
 454 and civilian applications. *Earth System Science Data Discussions*, *2022*, 1–40.
 455 Retrieved from <https://essd.copernicus.org/preprints/essd-2021-441/>
 456 doi: 10.5194/essd-2021-441
- 457 Krishnamoorthy, S., Bowman, D. C., Komjathy, A., Pauken, M. T., & Cutts, J. A.
 458 (2020a, October). Origin and mitigation of wind noise on balloon-borne in-
 459 frasound microbarometers. *The Journal of the Acoustical Society of America*,
 460 *148*(4), 2361–2370. doi: 10.1121/10.0002356
- 461 Krishnamoorthy, S., Bowman, D. C., Komjathy, A., Pauken, M. T., & Cutts, J. A.
 462 (2020b, October). Origin and mitigation of wind noise on balloon-borne in-
 463 frasound microbarometers. *The Journal of the Acoustical Society of America*,
 464 *148*(4), 2361–2370. doi: 10.1121/10.0002356
- 465 Krishnamoorthy, S., Lai, V. H., Komjathy, A., Pauken, M. T., Cutts, J. A., Gar-
 466 cia, R. F., ... Cadu, A. (2019). Aerial Seismology Using Balloon-Based
 467 Barometers. *IEEE Transactions on Geoscience and Remote Sensing*, 1–11.
 468 Retrieved from <https://ieeexplore.ieee.org/document/8809415/> doi:
 469 10.1109/TGRS.2019.2931831
- 470 Marty, J. (2019). The IMS infrasound network: Current status and technological de-
 471 velopments. In A. Le Pichon, E. Blanc, & A. Hauchecorne (Eds.), *Infrasound
 472 monitoring for atmospheric studies: Challenges in middle atmosphere dynam-
 473 ics and societal benefits* (pp. 3–62). Cham: Springer International Publishing.
 474 doi: 10.1007/978-3-319-75140-5_1
- 475 Massman, W. J. (1978, September). On the Nature of Vertical Oscillations of Con-
 476 stant Volume Balloons. *Journal of Applied Meteorology*, *17*(9), 1351–1356. doi:
 477 10.1175/1520-0450(1978)017<1351:OTNOVO>2.0.CO;2
- 478 Matoza, R. S., Fee, D., Assink, J. D., Jezzi, A. M., Green, D. N., Kim, K., ... Wil-
 479 son, D. C. (2022). Atmospheric waves and global seismoacoustic observations
 480 of the january 2022 hunga eruption, tonga. *Science*, *0*(0), eeeeeeeeeee. Re-
 481 trieved from <https://www.science.org/doi/abs/10.1126/science.abo7063>
 482 doi: 10.1126/science.abo7063
- 483 Matoza, R. S., Fee, D., Garcés, M. A., Seiner, J. M., Ramón, P. A., & Hedlin,
 484 M. a. H. (2009). Infrasonic jet noise from volcanic eruptions. *Geophysical
 485 Research Letters*, *36*(8). doi: 10.1029/2008GL036486
- 486 Millán, L., Santee, M. L., Lambert, A., Livesey, N. J., Werner, F., Schwartz, M. J.,
 487 ... Froidevaux, L. (2022). The Hunga Tonga-Hunga Ha’apai Hydration of
 488 the Stratosphere. *Geophysical Research Letters*, *49*(13), e2022GL099381. doi:
 489 10.1029/2022GL099381
- 490 Picone, J. M., Hedin, A. E., Drob, D. P., & Aikin, A. C. (2002). NRLMSISE-00
 491 empirical model of the atmosphere: Statistical comparisons and scientific is-
 492 sues. *Journal of Geophysical Research: Space Physics*, *107*(A12), SIA 15-1-SIA
 493 15-16. doi: 10.1029/2002JA009430
- 494 Pierce, A. D., & Posey, J. W. (1971, December). Theory of the Excitation
 495 and Propagation of Lamb’s Atmospheric Edge Mode from Nuclear Ex-
 496 plosions. *Geophysical Journal International*, *26*(1-4), 341–368. doi:

- 10.1111/j.1365-246X.1971.tb03406.x
- Podglajen, A., Hertzog, A., Plougonven, R., & Legras, B. (2016). Lagrangian temperature and vertical velocity fluctuations due to gravity waves in the lower stratosphere. *Geophysical Research Letters*, *43*(7), 3543–3553. doi: 10.1002/2016GL068148
- Podglajen, A., Hertzog, A., Plougonven, R., & Žagar, N. (2014). Assessment of the accuracy of (re)analyses in the equatorial lower stratosphere. *Journal of Geophysical Research: Atmospheres*, *119*(19), 11,166–11,188. doi: 10.1002/2014JD021849
- Poli, P., & Shapiro, N. M. (2022). Rapid Characterization of Large Volcanic Eruptions: Measuring the Impulse of the Hunga Tonga Ha’apai Explosion From Teleseismic Waves. *Geophysical Research Letters*, *49*(8), e2022GL098123. doi: 10.1029/2022GL098123
- Proud, S. R., Prata, A., & Schmauss, S. (2022). The January 2022 eruption of hunga tonga-hunga haapai volcano reached the mesosphere. *Earth and Space Science Open Archive*, 11. Retrieved from <https://doi.org/10.1002/essoar.10511092.1> doi: 10.1002/essoar.10511092.1
- Sellitto, P., Podglajen, A., Belhadji, R., Boichu, M., Carboni, E., Cuesta, J., ... Legras, B. (2022). *The unexpected radiative impact of the Hunga Tonga eruption of January 15th, 2022*. doi: 10.21203/rs.3.rs-1562573/v1
- Vergoz, J., Hupe, P., Listowski, C., Le Pichon, A., Garcés, M. A., Marchetti, E., ... Mialle, P. (2022, August). IMS observations of infrasound and acoustic-gravity waves produced by the January 2022 volcanic eruption of Hunga, Tonga: A global analysis. *Earth and Planetary Science Letters*, *591*, 117639. doi: 10.1016/j.epsl.2022.117639
- Vincent, R. A., & Hertzog, A. (2014, April). The response of superpressure balloons to gravity wave motions. *Atmospheric Measurement Techniques*, *7*(4), 1043–1055. doi: 10.5194/amt-7-1043-2014
- Watson, L. M., Iezzi, A. M., Toney, L., Maher, S. P., Fee, D., McKee, K., ... Johnson, J. B. (2022, April). Volcano infrasound: Progress and future directions. *Bulletin of Volcanology*, *84*(5), 44. doi: 10.1007/s00445-022-01544-w
- Waxler, R., & Assink, J. (2019). Propagation Modeling Through Realistic Atmosphere and Benchmarking. In A. Le Pichon, E. Blanc, & A. Hauchecorne (Eds.), *Infrasound Monitoring for Atmospheric Studies: Challenges in Middle Atmosphere Dynamics and Societal Benefits* (pp. 509–549). Cham: Springer International Publishing. doi: 10.1007/978-3-319-75140-5_15
- Waxler, R., Hetzer, C., Assink, J., & Velea, D. (2021, September). *Chetzer-ncpa/ncpaprop-release: NCPAprop v2.1.0*. Zenodo. doi: 10.5281/zenodo.5562713
- Woulff, G., & McGetchin, T. R. (1976, June). Acoustic Noise from Volcanoes: Theory and Experiment. *Geophysical Journal International*, *45*(3), 601–616. doi: 10.1111/j.1365-246X.1976.tb06913.x
- Wright, C. J., Hindley, N. P., Alexander, M. J., Barlow, M., Hoffmann, L., Mitchell, C. N., ... Yue, J. (2022, June). Surface-to-space atmospheric waves from Hunga Tonga-Hunga Ha’apai eruption. *Nature*, 1–3. doi: 10.1038/s41586-022-05012-5
- Young, E. F., Bowman, D. C., Lees, J. M., Klein, V., Arrowsmith, S. J., & Ballard, C. (2018, May). Explosion-Generated Infrasound Recorded on Ground and Airborne Microbarometers at Regional Distances. *Seismological Research Letters*, *89*(4), 1497–1506. doi: 10.1785/0220180038
- Yuen, D. A., Scruggs, M. A., Spera, F. J., Zheng, Y., Hu, H., McNutt, S. R., ... Tanioka, Y. (2022, March). Under the Surface: Pressure-Induced Planetary-Scale Waves, Volcanic Lightning, and Gaseous Clouds Caused by the Submarine Eruption of Hunga Tonga-Hunga Ha’apai Volcano Provide an Excellent Research Opportunity. *Earthquake Research Advances*, 100134. doi:

